Progress In Electromagnetics Research M, Vol. 58, 135–145, 2017

Study of Effect of Numerical Breast Phantom Heterogeneity on Dielectric Profile Reconstruction Using Microwave Imaging

Hardik N. Patel* and Deepak K. Ghodgaonkar

Abstract—Human breast is a heterogeneous medium for microwave signal. Breast cancer detection using microwave imaging is done based on signal scattered by breast tissues at different frequencies. Wave propagation direction is extremely important in heterogeneous medium like human breast. In this paper, the effect of wave propagation direction on the dielectric profile reconstruction is simulated in the presence of noise. X and Y directed transverse electric (TE) waves are considered for numerical breast phantom heterogeneity exploitation. Wave propagating in Y direction results into better dielectric profile reconstruction than X directed wave. Signal to noise ratio is very crucial for microwave imaging because information resides in low power scattered electric signal. Results show that SNR of at least 30 dB is required to detect cancer by solving extremely under-determined system of scattering equations.

1. INTRODUCTION

Microwave imaging of breast for tumor detection is a very promising technique. It has evolved faster in last three decades due to rapid increase in computational capability. Low power microwave signal is incident on breast, and according to dielectric profile of breast tissues, the incident wave is scattered by them. These scattered field measurements can be done practically or theoretically. Theoretical measurements are often known as forward simulation. Once scattered field at antennas is known, unknown dielectric profiles of breast tissues are determined by solving inverse scattering problem.

In this paper, the effect of wave propagation on dielectric profile reconstruction is simulated in the presence of noise. Transverse electric wave is considered in X and Y directions for numerical breast phantom heterogeneity exploitation. X directed TE wave has electric field components in Y, Z directions and all magnetic field components. Y directed TE wave has electric field components in X, Z directions and all magnetic field components. FDTD implementation basics are covered in [1, 2]. FDTD confocal system is first applied to breast cancer detection in [3]. Space time beam forming method is given for early breast cancer detection [4]. Experimental setup for multi-layer breast phantom is described in [5]. Complex permittivity of normal breast tissues obtained from reduction surgeries are measured in [6] for 0.5 GHz–20 GHz. Complex permittivity of normal, benign, and malignant breast tissues obtained from reduction surgeries are measured in [7] for 0.5 GHz–20 GHz. Breast tissues are polarized due to incident microwave signal. Breast tissues permittivity is a function of frequency which leads to dispersion. This effect is best described by Debye model. Debye models for healthy and malignant breast tissues are given in [8]. Anatomically realistic breast phantoms are used in this paper [9]. Numerical breast phantoms are available in the repository of University of Wisconsin [9]. Three-dimensional microwave imaging using multi-frequency inverse scattering technique is given with great detail in [10]. It also describes global optimization technique conjugate gradient to solve inverse scattering problem. Inverse scattering problem of microwave breast imaging is solved using 3D level set algorithm in [11]. This algorithm is computationally efficient as compared to adjoint method. The

---

Received 13 April 2017, Accepted 14 June 2017, Scheduled 13 July 2017

* Corresponding author: Hardik N. Patel (hardikec2003@gmail.com).

The authors are with the RF & Wireless Lab, DA-IICT, Gandhinagar, Gujarat, India.

research works of [10] and [11] have considered only Z directed source to make the calculation of Green's function simple. They have not considered X and Y directed sources. We are claiming that source direction also affects the reconstruction of dielectric properties. Source direction is important because of breast heterogeneity. This paper is a simulation based study of effect of numerical breast phantom heterogeneity on reconstruction of breast dielectric profile. Breast anatomy is given in [12], which clearly supports our assumption of considering only fibro-glandular and fatty (adipose) tissues in this study. Gauss-Newton and CGLS iterative algorithms are given in [13], which do not use any shape related parameters like level set functions. Level set functions are useful in the 3D reconstruction of breast tissues. The above algorithms do not reconstruct tissues' distribution effectively. Measurement and analysis of microwave signal transmission and reflection due to breast are given in [14, 15]. The reflection and transmission coefficient results of [14] and [15] are quite motivating. These results clearly show the matching between simulation and measurement. Our reflection coefficient results are quite good as compared to simulation results of [14, 15]. UPML equations are derived in [16] with all necessary details. These equations are used in PML region of this study. FDTD parameters are calculated using the equations given in [17]. Breast tumor location and shape reconstruction are done using gradient descent iterative algorithm in [18]. Shape reconstruction of [18] is also poor.

In this paper, effect of numerical breast phantom heterogeneity on dielectric profile reconstruction using microwave imaging is simulated. Numerical breast phantom is heterogeneous medium, so reflected power is different in different directions. Electric field update equations for numerical breast phantom region and perfectly matched layer region are different. Polarization and dispersion effects are considered only for numerical breast phantom using Debye model. Numerical breast phantom is immersed in oil medium to get best matching conditions. Forward 3D FDTD total field/scatter field (TF/SF) simulation is done to calculate normalized reflected power over 0.5 GHz to 2.5 GHz. Now, noise is added to the total electric field, and inverse problem is formulated. The formulated inverse problem is solved using 3D level set based gradient descent method. Next sections are dielectric properties of breast tissues, numerical breast phantom and antenna placement surrounding breast, electric field update equations for forward simulation, inverse problem formulation in frequency domain, simulation parameters, results, and conclusion.

1.1. Dielectric Properties of Breast Tissues

Breast anatomy is extremely important for understanding from imaging point of view. Breast anatomy is covered with great detail in [12] for researchers. Breast consists of skin layer, fatty tissue layer, fibro-glandular tissues, chest wall (ribs and pectoral muscles), and blood vessels. Coopers ligament and lymph nerves are present in the above tissues. Tissues are formed by same type of cells. The dielectric properties of healthy breast tissues are different at microwave frequencies [6]. Complex relative permittivity of breast tissues is a function of frequency which generates dispersion. Dispersive nature of breast tissues is easily incorporated using Debye model. Single pole Debye model is given below.

$$\epsilon(\omega) = \epsilon_\infty + \frac{\Delta\epsilon}{j\omega\tau} + \frac{\sigma_s}{j\omega\epsilon_0} \tag{1}$$

In Eq. (1), ϵ_∞ is the infinite frequency permittivity, $\Delta\epsilon$ the difference between static permittivity (ϵ_s) and infinite frequency permittivity (ϵ_∞), σ_s the static conductivity, and τ the relaxation time constant which is 15 ps for all breast tissues. Relaxation time constant is spatially invariant. In order to reduce number of variables per voxel, τ is fixed at 15 ps. This assumption is valid because of minor variations in τ throughout the imaging domain for 0.5 GHz to 2.5 GHz frequency range.

1.2. Numerical Breast Phantom and Antenna Placement Surrounding Breast

Simulation is done using class 3 numerical breast phantom developed in [9]. Y-Z, X-Z, and X-Y views are shown in Fig. 1.

White color represents fibro-glandular tissues, and black or gray color represents adipose tissues. MRI derived numerical breast phantom is used to make simulation more realistic. Fig. 2 shows antenna placement surrounding numerical breast phantom. There are five rings of antennas around numerical

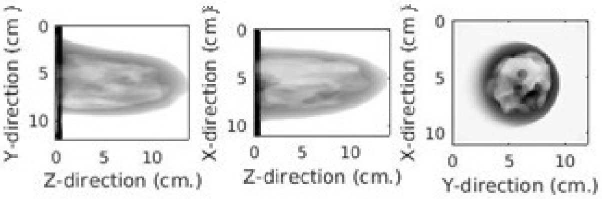

Figure 1. Y-Z, X-Z and X-Y view of class 3 MRI derived numerical breast phantom.

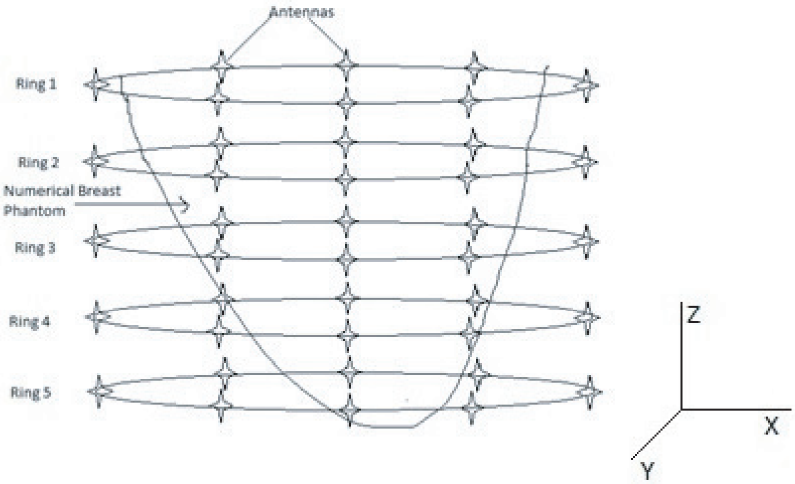

Figure 2. Antenna placement surrounding the numerical breast phantom.

breast phantom. Each ring has eight infinitesimal dipoles of area 2 cm × 2 cm, which lead to 40 antennas in the system.

2. ELECTRIC FIELD UPDATE EQUATIONS FOR FORWARD SIMULATION

Electric field update equations for numerical breast phantom region and PML region are given in this section.

2.1. Electric Field Update Equations for Numerical Breast Phantom Region

Maxwell's equation is given by Eq. (2) after incorporating Debye model in it [17].

$$\vec{\nabla} \times \vec{H} = \epsilon_0 \epsilon_\infty j\omega \vec{E} + \sigma_s \vec{E} + j\omega\epsilon_0 \frac{\Delta\epsilon}{1 + j\omega\tau} \vec{E} \tag{2}$$

In Eq. (2), $\vec{H}$ is the magnetic field intensity and $\vec{E}$ the electric field intensity. Equation (2) is converted into time domain using FDTD. Now applying simple algebra, Equation (3) is obtained.

$$\vec{E}_{t+\Delta t} = me1 \cdot \vec{E}_t + me2 \cdot \left[\left(2\Delta x \cdot \vec{\nabla} \times \vec{H} \right) - \left(\eta_0 \cdot (1 + mj1) \cdot \Delta x \cdot \vec{J_P} \right) \right] \tag{3}$$

In Eq. (3), $\vec{E}_{t+\Delta t}$ is the electric field intensity at current time step, $\vec{E}_t$ the electric field intensity at previous time step, $\vec{\nabla} \times \vec{H}$ the curl of magnetic field intensity, $\vec{J_P}$ the polarization current density, and Δx the size of voxel in x direction. Coefficient $mj1$ is given by Eq. (7). Coefficient me1 is given by Eq. (4).

$$me1 = \frac{1 - \dfrac{\sigma_s \Delta t}{2\epsilon_0 \epsilon_\infty} + \dfrac{mj2 \cdot \Delta t}{2\epsilon_0 \epsilon_\infty \Delta x}}{1 + \dfrac{\sigma_s \Delta t}{2\epsilon_0 \epsilon_\infty} + \dfrac{mj2 \cdot \Delta t}{2\epsilon_0 \epsilon_\infty \Delta x}} \tag{4}$$

In Eq. (4), Δt is the time step. Coefficient me2 is given by Eq. (5). Coefficient $mj2$ is given by Eq. (8).

$$me2=\frac{c_0\Delta t}{2\Delta x\cdot\epsilon_\infty\left(1+\dfrac{\sigma_s\Delta t}{2\epsilon_0\epsilon_\infty}+\dfrac{mj2\cdot\Delta t}{2\epsilon_0\epsilon_\infty\Delta x}\right)}\tag{5}$$

In Eq. (5), c_0 is the speed of light. Polarization current density update equation is given by Eq. (6). Equations (3), (4) and (5) are implemented for x, y and z components of electric field vector.

$$\vec{J}_P^{t+\Delta t}=mj1\cdot\vec{J}_P^{t}+\frac{mj2\cdot\left(\vec{E}_{t+\Delta t}-\vec{E}_t\right)}{\Delta x}\tag{6}$$

In Equation (6), $\vec{J}_P^{t+\Delta t}$ is the polarization current density at current time step and $\vec{J}_P^{t}$ the polarization density at previous time step. Coefficient $mj1$ is given by Eq. (7).

$$mj1=\frac{1-\dfrac{1}{2N_t}}{1+\dfrac{1}{2N_t}}\tag{7}$$

In Eq. (7), relaxation time constant $\tau=N_t\Delta t$. Coefficient $mj2$ is given by Eq. (8).

$$mj2=\frac{\epsilon_0\Delta\epsilon\Delta x}{N_t\Delta\cdot\left(1+\dfrac{1}{2N_t}\right)}\tag{8}$$

Equations (6), (7) and (8) are implemented for x, y and z components of the polarization current density vector. Polarization current density vector is updated before updating electric field vector.

2.2. Electric Field Update Equations for PML Region

Electric field update equation derivation for PML region is given in [16,17]. Electric field update equation for PML region is given by Eq. (9).

$$\vec{D}_{t+\Delta t}=mdx1\cdot\vec{D}_t+mdx2\cdot\left(\vec{\nabla}\times\vec{H}\right)_x+mdx3\cdot(Ich)_x+mdx4\cdot(ID)_x\tag{9}$$

In Equation (9), $\vec{D}_{t+\Delta t}$ is the electric field density (x component) at current time step, $\vec{D}_t$ the electric field density (x component) at previous time step, $(\vec{\nabla}\times\vec{H})_x$ the x component of curl of vector H, $(Ich)_x$ the x component of integration of curl of vector H, and $(ID)_x$ the x component of integration of electric field density vector D. Coefficient $mdx0$ is given by Eq. (10).

$$mdx0=\frac{1}{\Delta t}+\frac{\sigma_y+\sigma_z}{2\epsilon_0}+\frac{\sigma_y\cdot\sigma_z\cdot\Delta t}{4\epsilon_0^2}\tag{10}$$

In Equation (10), conductivities in y and z directions are represented by σ_y and σ_z. These conductivity values are non-zero only in the PML region. Sometimes they are known as fictitious conductivity. Coefficient $mdx1$ is given by Eq. (11).

$$mdx1=\frac{1}{mdx0}\left(\frac{1}{\Delta t}-\frac{\sigma_y+\sigma_z}{2\epsilon_0}-\frac{\sigma_y\cdot\sigma_z\cdot\Delta t}{4\epsilon_0^2}\right)\tag{11}$$

Coefficient $mdx2$ is given by Eq. (12).

$$mdx2=\frac{c_0}{mdx0}\tag{12}$$

In Equation (12), c_0 is the speed of light. Coefficient $mdx3$ is given by Eq. (13).

$$mdx3=\frac{c_0\cdot\Delta t\cdot\sigma_x}{mdx0\cdot\epsilon_0}\tag{13}$$

In Equation (13), σ_x is the x component of conductivity. Coefficient $mdx4$ is given by Eq. (14).

$$mdx4=\frac{\Delta t\cdot\sigma_y\cdot\sigma_z}{mdx0\cdot\epsilon_0^2}\tag{14}$$

Equations (9) to (14) are implemented for x, y and z components of electric field density vector D in PML region.

3. INVERSE PROBLEM FORMULATION IN FREQUENCY DOMAIN

The total electric field is known at the antenna locations due to forward simulation. Scattered field at antenna locations is calculated using Eq. (15).

$$\vec{E}^s(\vec{r}) = \iiint G(\vec{r}, \vec{r}') \cdot \vec{J}(\vec{r}')dv' \tag{15}$$

In Eq. (15), $\vec{E}^s(\vec{r})$ is the scattered electric field at antenna locations $\vec{r}$, $G(\vec{r}, \vec{r}')$ the Green's function for homogeneous background medium, and $\vec{J}(\vec{r}')$ the polarization current density. Equation (16) is obtained by substituting polarization current density into Eq. (15).

$$\vec{E}^s(\vec{r}) = \omega^2\mu \iiint G(\vec{r}, \vec{r}') \cdot \vec{E}_t(\vec{r}') \left[\epsilon(\vec{r}') - \epsilon^b(\vec{r})\right] dr' \tag{16}$$

In Eq. (16), $\epsilon(\vec{r}') - \epsilon^b(\vec{r})$ is permittivity contrast (with respect to homogeneous background medium), and $\vec{E}_t(\vec{r}')$ is the total electric field intensity at location $\vec{r}'$. Linear approximation of scattering equation of Eq. (16) is obtained using [10]. Numerical breast phantom is discritized in K voxels. There are 40 antennas surrounding breast as shown in Fig. 2. Each antenna works as a transmitter or a receiver. One antenna transmits microwave signal on breast while other antennas receive scattered signal due to breast tissues. This process is repeated for each antenna present in the system. Let us consider that there are N antennas in the system. There is F number of frequencies. Ideally, there are N^2F measurements possible. Antenna is reciprocal so some measurements can be neglected. There are only $(N(N-1)/2)F$ measurements possible after removing redundancy. There are $N-1$ receivers when the first antenna transmits. There are $N-2$ receivers when the second antenna transmits. By this way, there are channels among transmitters and receivers. By considering N antennas, D number of channels, F number of frequencies, and K voxels, Eq. (17) is obtained.

$$\mu\epsilon_0 \sum_{p=1}^{D}\sum_{l=1}^{F}\sum_{j=1}^{K} \omega_l^2 \left((\delta(\epsilon_\infty))_j + \frac{(\delta(\Delta\epsilon))_j}{1+j\omega_l\tau} + \frac{(\delta(\sigma_s))_j}{j\omega\epsilon_0} \right) \cdot \left(E_x^t(\vec{r}_j|\vec{r}_m, \omega_l) \cdot IG_x(\vec{r}_n|\vec{r}_j, \omega_l) \right)_p \tag{17}$$

In Eq. (17), $\delta(\epsilon_\infty) = (\epsilon_\infty)_k - (\epsilon_\infty)_b$ is the difference between the kth voxel infinite frequency permittivity and background medium infinite frequency permittivity, and $\delta(\Delta\epsilon) = (\Delta\epsilon)_k - (\Delta\epsilon)_b$ and $\delta(\sigma_s) = (\sigma_s)_k - (\sigma_s)_b$ are defined the same as above. In Eq. (17), $E_x^t(\vec{r}_j|\vec{r}_m, \omega_l)$ is the x direction electric field present at the jth voxel location due to the transmitter at location $\vec{r}_m$ for angular frequency ω_l; $IG_x(\vec{r}_n|\vec{r}_j, \omega_l)$ is the x direction component of the integration of the Green's function at angular frequency ω_l; $\vec{r}_n$ represents receiver location; p represents particular channel number. Now, Eq. (17) can be represented in the matrix form as shown by Eq. (18). By comparing Eq. (18) with $Ax = b$, A is of size $2MF \times 3K$, where Re(·) represents real part; Im(·) represents imaginary part; size of x is $3K \times 1$; size of b is $2MF \times 1$. There are total $2MF$ equations and $3K$ unknowns. In our system, there are 40 antennas, number of frequencies $F = 18$, and $K = 64000$.

$$\begin{bmatrix} \mathrm{Re}(A_1^\infty) & \mathrm{Re}(A_1^\Delta) & \mathrm{Re}(A_1^\sigma) \\ \mathrm{Im}(A_1^\infty) & \mathrm{Im}(A_1^\Delta) & \mathrm{Im}(A_1^\sigma) \\ & \vdots & \\ \mathrm{Re}(A_M^\infty) & \mathrm{Re}(A_M^\Delta) & \mathrm{Re}(A_M^\sigma) \\ \mathrm{Im}(A_M^\infty) & \mathrm{Im}(A_M^\Delta) & \mathrm{Im}(A_M^\sigma) \end{bmatrix} \begin{bmatrix} \delta(\epsilon_\infty) \\ \delta(\Delta\epsilon) \\ \delta(\sigma_s) \end{bmatrix} = \begin{bmatrix} \mathrm{Re}(E_1^s) \\ \mathrm{Im}(E_1^s) \\ \vdots \\ \mathrm{Re}(E_M^s) \\ \mathrm{Im}(E_M^s) \end{bmatrix} \tag{18}$$

There are 28,080 equations and 192000 unknowns in our system. It means that this approximated linear system of Eq. (18) is underdetermined. In Eq. (18), each element is represented by the matrix of Eq. (19), and scattered field is represented by Eq. (20).

$$A_d^p = \begin{bmatrix} C_p(\omega_1)\left[a_1^d(\omega_1)\dots a_k^d(\omega_1)\right] \\ \vdots \\ C_p(\omega_F)\left[a_1^d(\omega_F)\dots a_k^d(\omega_F)\right] \end{bmatrix} \tag{19}$$

where, $a_k^d(\omega_1) = \omega_1^2 \mu \epsilon_0 \cdot E_x^t(\vec{r}_j|\vec{r}_m, \omega_1) \cdot IG_x(\vec{r}_n|\vec{r}_j, \omega_1)$ and d represents particular channel number, $C_\infty(\omega) = 1$, $C_\Delta(\omega) = (1 + j\omega\tau)^{-1}$, $C_\sigma(\omega) = (j\omega\epsilon_0)^{-1}$

Equation (21) represents cost function. In Eq. (21), F is the number of frequencies, M the number of measurements, $\vec{r}_n$ the receiver location for particular channel, and ω_f the angular frequency. Scattered electric field matrix of Eq. (20) is known due to forward simulation. Left-hand side matrix A of Eq. (18) is also known. Permittivity contrast profile column matrix x is only unknown in Eq. (18). System of scattering equations is converted into matrices as shown by Equations (17) and (18). The unknown vector of Equation (18) is in terms of Debye parameters. We are dealing with real numbers in this type of modelling. Real number operations are faster than complex number operations, so the system represented by Eq. (18) is computationally efficient. Ultimately, we reconstruct Debye parameter unknowns instead of complex permittivity reconstruction.

$$E_d^s = \begin{bmatrix} E_x^t(\vec{r}_n|\vec{r}_m, \omega_1) - E_x^i(\vec{r}_n|\vec{r}_m, \omega_1) \\ \vdots \\ E_x^t(\vec{r}_n|\vec{r}_m, \omega_F) - E_x^i(\vec{r}_n|\vec{r}_m, \omega_F) \end{bmatrix} \tag{20}$$

$$C(\epsilon) = \frac{1}{2} \sum_{f=1}^{F} \sum_{n=1}^{M} \left| E_m^t(\vec{r}_n, \omega_f) - E_r^t\left(\vec{r}_n, \omega_f, \epsilon\left(\vec{r}'\right)\right)\right) \tag{21}$$

In this paper, Eq. (21) is minimized using 3D level set based gradient descent algorithm [11].

3.1. Noise Consideration

Additive white Gaussian noise is added in scattered field using Eq. (22). After adding noise, inverse problem is solved.

$$Ax = b + n \tag{22}$$

In above equation, n is the AWGN noise vector with different signal to noise ratios. SNR varies from 10 db to 50 db. RMSE in Debye parameters is calculated using Eq. (23).

$$RMSE = \sqrt{\frac{\sum_{i=1}^{K} (\epsilon_i - \hat{\epsilon}_i)^2}{K}} \tag{23}$$

In Eq. (23), ϵ_i is the Debye parameter original value of the ith voxel, and $\hat{\epsilon}_i$ is the Debye parameter reconstructed value of the ith voxel. K is the total number of voxels used in model.

4. SIMULATION PARAMETERS

Debye parameters' values are given for different breast tissues in Table 1. These values are valid for 0.5 GHz to 3 GHz. For simplicity, only two major types of tissues are considered in class 3 numerical breast phantom. Tumour is not there in MRI derived numerical breast phantom used in this study, so tumour location is assumed here. Tumour is assumed in glandular tissues because it starts in this type of tissues.

Coronal cross sections of numerical breast phantom with ϵ_∞, $\Delta\epsilon$ and σ_s original profiles are shown in Figs. 3, 4, and 5, respectively. Malignant tumor is assumed in the fibro-glandular tissues. Fig. 3, Fig. 4, and Fig. 5 profiles are used to get scattered field at antenna locations. Noise is added to these field values before solving inverse scattering problem.

5. RESULTS

Normalized reflected power vs. frequency graph for different directions is shown in Fig. 6. It clearly shows several reflected power peaks at different frequencies. 3D FDTD simulation is done over 18 equally spaced discrete frequencies between 500 MHz and 2.5 GHz. Reconstructed Debye parameters profiles

Table 1. Debye parameters' values for different breast tissues.

Tissues	ϵ_∞	$\Delta\epsilon$	σ_s (s/m)
Adipose (fatty)	4.09	3.54	0.0842
Fibro-glandular	18.6	35.6	0.817
Skin	15.3	24.8	0.741
Tumor (assumed)	23.2	41	0.93
Immersion medium	2.6	0	0

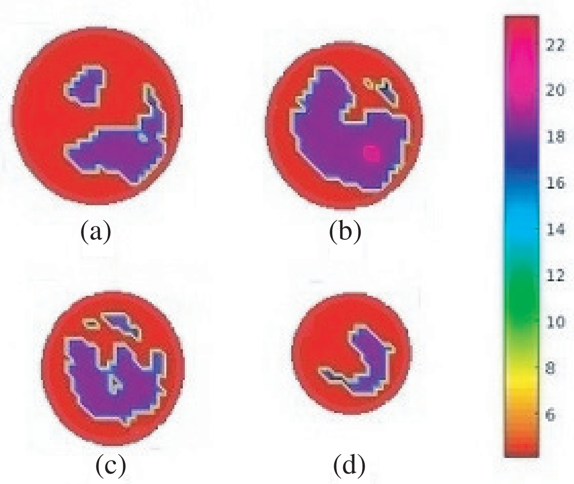

(a) (b) (c) (d)

Figure 3. Coronal cross section of class 3 breast phantom with original profile of ϵ_∞ at (a) 1.5 cm, (b) 3 cm, (c) 4.5 cm, (d) 6 cm. (Dark pink dot of (b) indicates malignant tumor tissues).

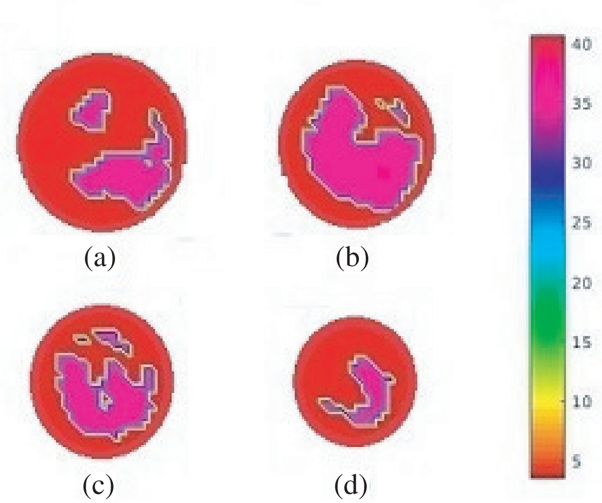

(a) (b) (c) (d)

Figure 4. Coronal cross section of class 3 breast phantom with original profile of $\Delta\epsilon$ at (a) 1.5 cm, (b) 3 cm, (c) 4.5 cm, (d) 6 cm. (Dark pink dot of (b) indicates malignant tumor tissues).

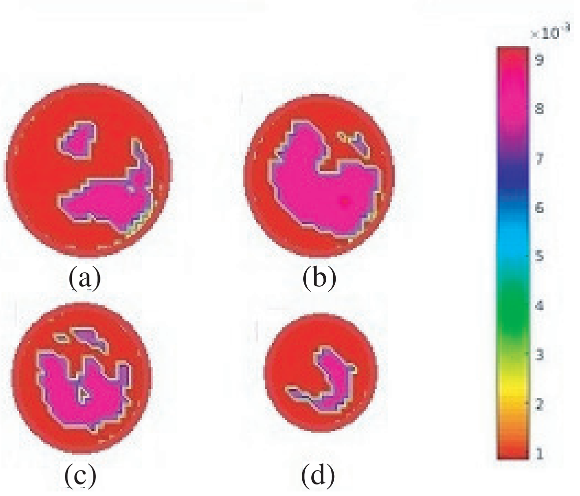

(a) (b) (c) (d)

Figure 5. Coronal cross section of class 3 breast phantom with original profile of σ_s at (a) 1.5 cm, (b) 3 cm, (c) 4.5 cm, (d) 6 cm. (Dark pink dot of (b) indicates malignant tumor tissues.

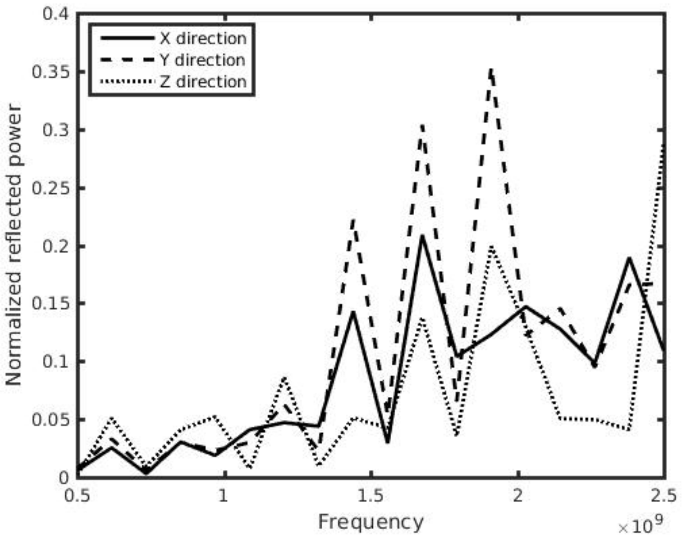

Figure 6. Normalized reflected power vs. frequency for different directions.

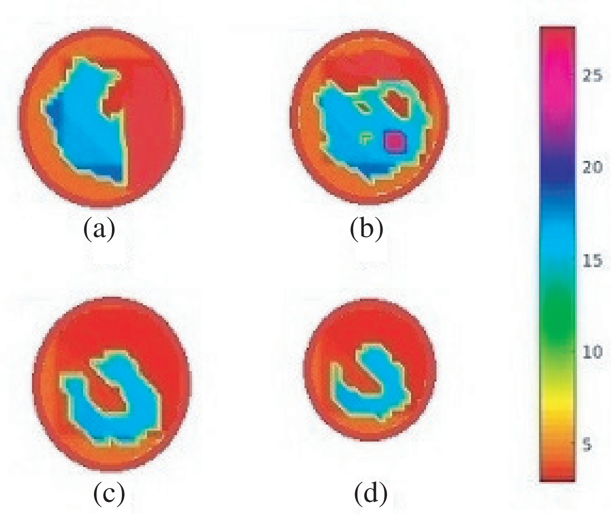

(a) (b)

(c) (d)

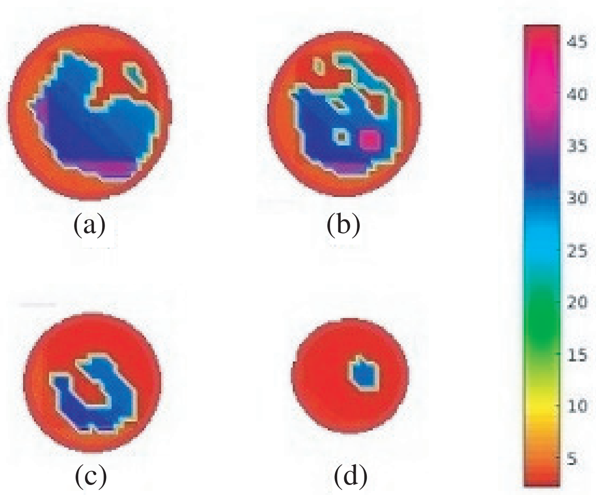

(a) (b)

(c) (d)

Figure 7. Coronal cross section of class 3 breast phantom with reconstructed profile of ϵ_∞ for X direction wave propagation at (a) 1.5 cm, (b) 3 cm, (c) 4.5 cm, (d) 6 cm. (SNR 40 dB).

Figure 8. Coronal cross section of class 3 breast phantom with reconstructed profile of $\Delta\epsilon$ for X direction wave propagation at (a) 1.5 cm, (b) 3 cm, (c) 4.5 cm, (d) 6 cm. (SNR 40 dB).

for x direction wave propagation are shown in Fig. 7, Fig. 8 and Fig. 9, respectively. Reconstructed Debye parameters profiles for y direction wave propagation are shown in Fig. 10, Fig. 11 and Fig. 12, respectively.

By comparing Fig. 7 with Fig. 3, it is clear that in the reconstruction of ϵ_∞ profile, its shape and values both are poor for x direction wave propagation. By comparing Fig. 8 with Fig. 4, it is clear that in the reconstruction of $\Delta\epsilon$ profile, its shape and values both are poor for x direction wave propagation.

By comparing Fig. 9 with Fig. 5, it is clear that in the reconstruction of σ_s profile, its shape and values both are poor for x direction wave propagation. By comparing Fig. 10 with Fig. 3 and Fig. 7, it is clear that in the reconstruction of ϵ_∞ profile, its shape and values both are better for y direction

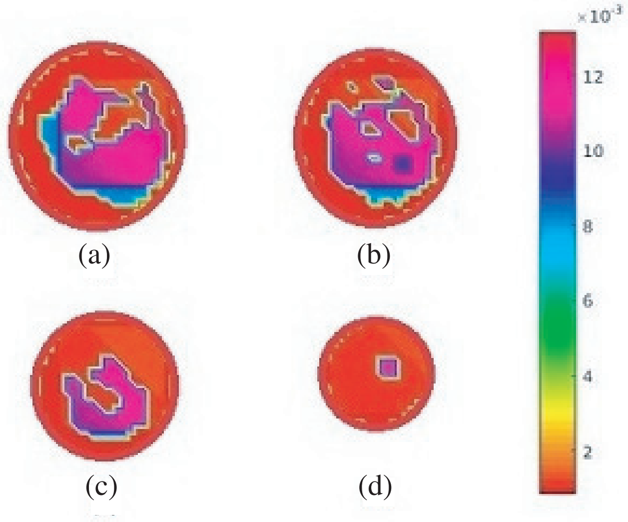

Figure 9. Coronal cross section of class 3 breast phantom with reconstructed profile of σ_s for X direction wave propagation at (a) 1.5 cm, (b) 3 cm, (c) 4.5 cm, (d) 6 cm. (SNR 40 dB).

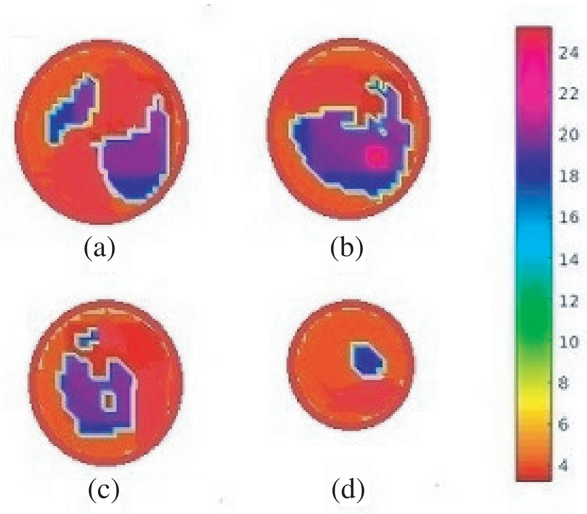

Figure 10. Coronal cross section of class 3 breast phantom with reconstructed profile of ϵ_∞ for Y direction wave propagation at (a) 1.5 cm, (b) 3 cm, (c) 4.5 cm, (d) 6 cm. (SNR 40 dB).

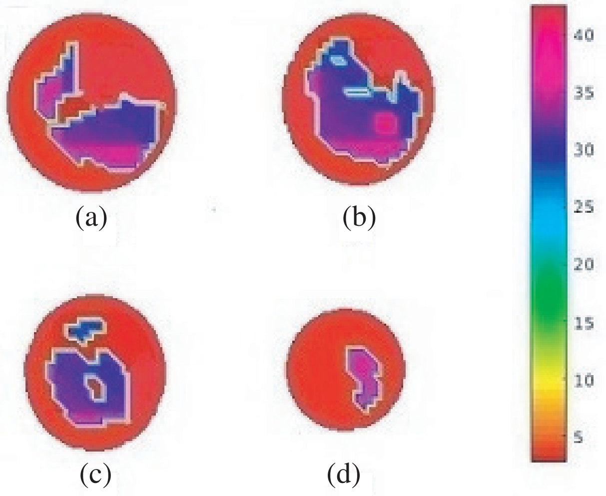

Figure 11. Coronal cross section of class 3 breast phantom with reconstructed profile of $\Delta\epsilon$ for Y direction wave propagation at (a) 1.5 cm, (b) 3 cm, (c) 4.5 cm, (d) 6 cm. (SNR 40 dB).

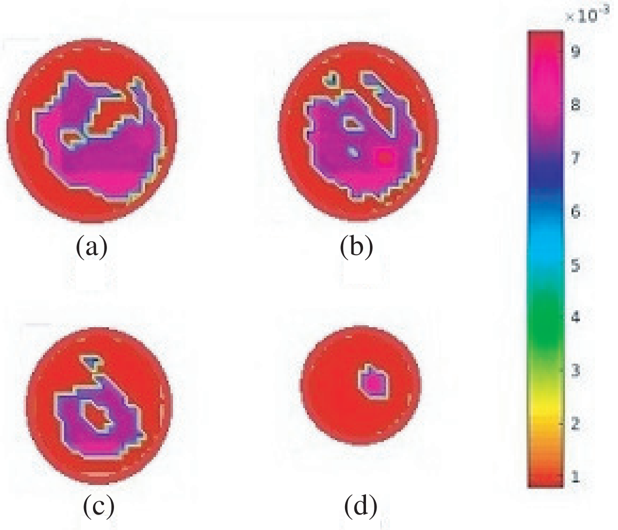

Figure 12. Coronal cross section of class 3 breast phantom with reconstructed profile of σ_s for Y direction wave propagation at (a) 1.5 cm, (b) 3 cm, (c) 4.5 cm, (d) 6 cm. (SNR 40 dB).

propagation than for x direction propagation. By comparing Fig. 11 with Fig. 4 and Fig. 8, it is clear that in the reconstruction of $\Delta\epsilon$ profile, its shape and values both are better for y direction propagation than for x direction propagation.

By comparing Fig. 12 with Fig. 5 and Fig. 9, it is clear that in the reconstruction of σ_s profile, its shape and values both are better for y direction propagation than for x direction propagation. Fig. 13 shows RMSE in ϵ_∞ vs. SNR for X and Y directions wave propagation. Better reconstruction

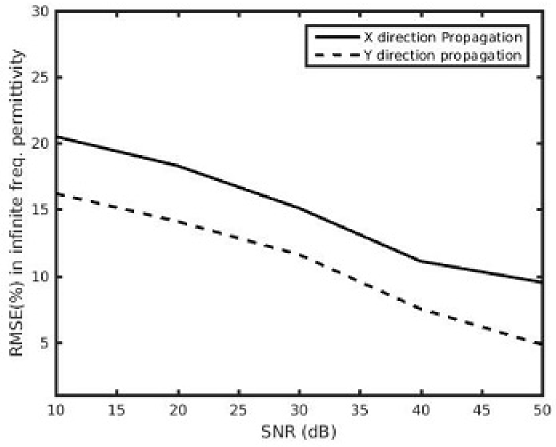

Figure 13. RMSE in ϵ_∞ vs. SNR for X and Y directions wave propagation.

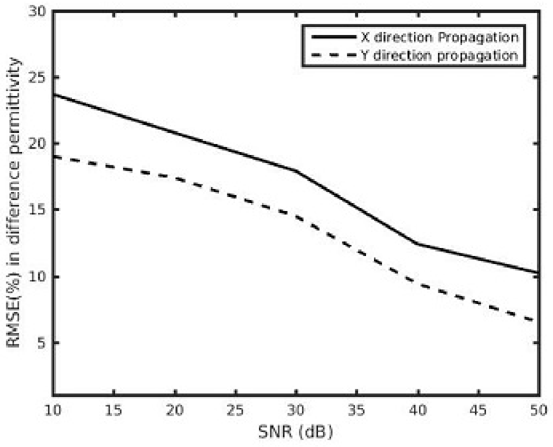

Figure 14. RMSE in $\Delta\epsilon$ vs. SNR for X and Y directions wave propagation.

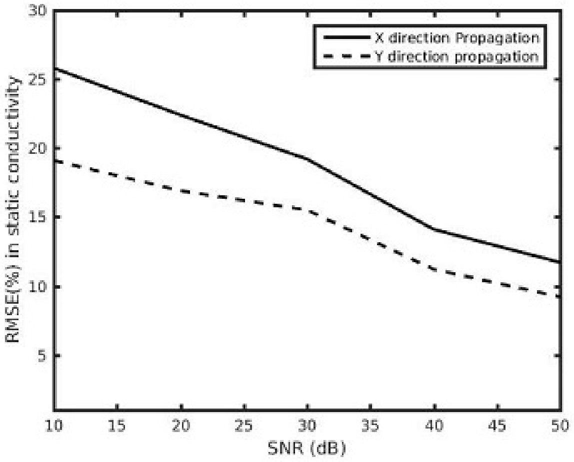

Figure 15. RMSE in σ_s vs. SNR for X and Y directions wave propagation.

of ϵ_∞ profile is achieved in the presence of noise for Y direction wave propagation than x direction wave propagation. Fig. 14 shows RMSE in $\Delta\epsilon$ vs. SNR for X and Y direction wave propagations. Better reconstruction of $\Delta\epsilon$ profile is achieved in the presence of noise for Y direction wave propagation than x direction wave propagation. Fig. 15 shows RMSE in σ_s vs. SNR for X and Y direction wave propagations. Better reconstruction of σ_s profile is achieved in the presence of noise for Y direction wave propagation than x direction wave propagation.

6. CONCLUSION

Results clearly show that y direction wave propagation through numerical breast phantom is better than x direction propagation. SNR of at least 30 dB is required to detect tumour properly. Breast heterogeneity varies with patients, so direction dependent analysis is extremely important. Reconstruction performance varies with wave direction due to numerical breast phantom heterogeneity. The effect of noise on dielectric reconstruction is less for Y direction wave propagation. The reason of better dielectric reconstruction for y direction is more reflected power in that direction. This study suggests that SNR of at least 30 dB is required to detect breast tumour properly using this reconstruction technique.

REFERENCES

1. Yee, K., "Numerical solution of initial boundary value problems involving Maxwell's equations in isotropic media," *IEEE Transactions on Antennas and Propagation*, Vol. 14, No. 3, 302–307, 1996.
2. Taflove, A., "Application of the finite-difference time-domain method to sinusoidal steady-state electromagnetic-penetration problems," *IEEE Transactions on Electromagnetic Compatibility*, Vol. 22, No. 3, 191–202, 1980.
3. Hagness, S. C., A. Taflove, and J. E. Bridges, "Two-dimensional FDTD analysis of a pulsed microwave confocal system for breast cancer detection: Fixed-focus and antenna-array sensors," *IEEE Transactions on Biomedical Engineering*, Vol. 45, No. 12, 1470–1479, 1998.
4. Bond, E. J., X. Li, S. C. Hagness, and B. D. Van Veen, "Microwave imaging via space-time beamforming for early detection of breast cancer," *IEEE Transactions on Antennas and Propagation*, Vol. 51, No. 8, 1690–1705, 2003.
5. Li, X., S. K. Davis, S. C. Hagness, D. W. Van der Weide, and B. D. Van Veen, "Microwave imaging via space-time beamforming: Experimental investigation of tumor detection in multilayer breast phantoms," *IEEE Transactions on Microwave Theory and Techniques*, Vol. 52, No. 8, 1856–1865, 2004.
6. Lazebnik, M., L. McCartney, D. Popovic, C. B. Watkins, M. J. Lindstrom, J. Harter, S. Sewall, A. Magliocco, J. H. Booske, M. Okoniewski, and S. C. Hagness, "A large-scale study of the ultrawideband microwave dielectric properties of normal breast tissue obtained from reduction surgeries," *Physics in Medicine and Biology*, Vol. 52, No. 10, 2637, 2007.
7. Lazebnik, M., D. Popovic, L. McCartney, C. B. Watkins, M. J. Lindstrom, J. Harter, S. Sewall, T. Ogilvie, A. Magliocco, T. M. Breslin, and W. Temple, "A large-scale study of the ultrawideband microwave dielectric properties of normal, benign and malignant breast tissues obtained from cancer surgeries," *Physics in Medicine and Biology*, Vol. 52, No. 20, 6093, 2007.
8. Lazebnik, M., M. Okoniewski, J. H. Booske, and S. C. Hagness, "Highly accurate Debye models for normal and malignant breast tissue dielectric properties at microwave frequencies," *IEEE Microwave and Wireless Components Letters*, Vol. 17, No. 12, 822–824, 2007.
9. Zastrow, E., S. K. Davis, M. Lazebnik, F. Kelcz, B. D. Van Veen, and S. C. Hagness, "Development of anatomically realistic numerical breast phantoms with accurate dielectric properties for modeling microwave interactions with the human breast," *IEEE Transactions on Biomedical Engineering*, Vol. 55, No. 12, 2792–2800, 2008.
10. Shea, J. D., P. Kosmas, S. C. Hagness, and B. D. Van Veen, "Three-dimensional microwave imaging of realistic numerical breast phantoms via a multiple-frequency inverse scattering technique," *Medical Physics*, Vol. 37, No. 8, 4210–4226, 2010.
11. Colgan, T. J., S. C. Hagness, and B. D. Van Veen, "A 3-D level set method for microwave breast imaging," *IEEE Transactions on Biomedical Engineering*, Vol. 62, No. 10, 2526–2534, 2015.
12. Jesinger, R. A., "Breast anatomy for the interventionalist," *Techniques in Vascular and Interventional Radiology*, Vol. 17, No. 1, 3–9, 2014.
13. Rubk, T., P. M. Meaney, P. Meincke, and K. D. Paulsen, "Nonlinear microwave imaging for breast-cancer screening using Gauss-Newton's method and the CGLS inversion algorithm," *IEEE Transactions on Antennas and Propagation*, Vol. 55, No. 8, 2320–2331, 2007.
14. Bourqui, J. and E. C. Fear, "Biological tissues assesment using transmitted microwave signals," *2014 8th European Conference on Antennas and Propagation (EuCAP)*, IEEE, 2014.
15. Bourqui, J., J. Garrett, and E. Fear, "Measurement and analysis of microwave frequency signals transmitted through the breast," *Journal of Biomedical Imaging*, 2012.
16. Gedney, S. D., "An anisotropic perfectly matched layer-absorbing medium for the truncation of FDTD lattices," *IEEE Transactions on Antennas and Propagation*, Vol. 44, No. 12, 1630–1639, 1996.
17. Taflove, A. and S. C. Hagness, *Computational Electrodynamics*, Artech House, 2005.
18. El-Shenawee, M. and E. L. Miller, "Spherical harmonics microwave algorithm for shape and location reconstruction of breast cancer tumor," *IEEE Transactions on Medical Imaging*, Vol. 25, No. 10, 1258–1271, 2006.